CHARACTERISTICS OF HEAT TRANSFER DURING COOLING DOWN PROCESS IN A SINGLE CARGO TANK OF LNG CARRIER

(DOI No: 10.3940/rina.ijme.2020.a3.588)

J J Deng, **L Y Song**, and **J Xu**, Zhejiang Ocean University, Zhoushan, The School of Port and Transportation Engineering, China, **B Liu**, Shijiazhuang Tiedao University, Shijiazhuang, The School of Mechanics Engineering, China, **J S Lu**, and **J W Zhang**, Zhejiang Ocean University, Zhoushan, The School of Port and Transportation Engineering, China

KEY DATES: Submitted: 14/06/19; Final acceptance: 21/06/20; Published: 07/10/20

SUMMARY

A deep understanding of heat transfer characteristics is essential in evaluating risk and putting forward any option for the Liquefied Natural Gas (LNG) tank cooling down process. A novel Computational Fluid Dynamics (CFD) model was built to perform the flow and heat transfer simulation of the process. The predicted results agreed well with the test data from a prototype LNG tank. Then the heat transfer characteristics of the process were analysed. It was found that the vapour temperature and density were linearly varying and became stable after 2.3 hours. A sudden pressure drop risk was identified during the process, which will cause the inwards collapse risk of the invar membrane. Then the proposals to prevent the risks of the inwards collapsing membrane are presented. The heat transfer characteristics of the vapour and different membrane layers were analysed in detail, and if the suggested option was to be implemented this could save about 39% of LNG consumed.

NOMENCLATURE

A	Contiguous area (m^2)
C_p	Specific heat capacity (J $kg^{-1}K^{-1}$)
D_ω	Cross-diffusion term of ω (kg m^{-3} s^{-2})
E_m	The volume average energy of mixture (J m^{-3})
$\vec{F}$	External body forces (N)
G_k	Generation of k (kg m^{-1} s^{-3})
G_ω	Generation of ω (kg m^{-3} s^{-2})
h_s	The sensible enthalpy of solid material (J kg^{-1})
h	Sensible enthalpy (J kg^{-1})
j	Either phase v or phase d
K	Heat transfer coefficient (W m^{-2} K^{-1})
k_{eff}	Effective heat transfer coefficient (W m^{-2} K^{-1})
k_s	The conductivity of solid material (w m^{-1} K^{-1})
L	The hydraulic diameter (m)
$\dot{m}_{vd}$	Phase transitions from vapour to droplet (kg s^{-1})
$\dot{m}_{dv}$	Phase transitions from droplet to vapour (kg s^{-1})
m_1	Injected LNG masses for each hour (kg)
m_2	Evapourated LNG masses for each hour (kg)
M_w	Molecular weight of the gas (kg $kmol^{-1}$)
N	Number of samples
Nu	Nusselt number
P_{op}	Operating pressure (Pa)
P	Static pressure (Pa)
R	Universal gas constant (J m^{-1} K^{-1})
Q	Net heat transfer rate between layers (W)
Q_1	Heat transfer rate to the current layer (W)
Q_2	Residual heat of the current layer (W)
Q_3	Heat transfer rate from the current layer (W)
S_T	Energy source term due to the phase transition (W)
T	Temperature (K)
T_1	Correlation data of temperature (K)
T_2	Baseline data of temperature (K)
T_{ref}	Reference temperature (K)
ΔT	Temperature difference of adjacent layers (K)
t	Cooling down time (s)
$\vec{v}_m$	Mixture's mass-averaged velocity (m s^{-1})
$\vec{v}_{dr,d}$	Drift velocity of phase d (m s^{-1})
Y_k	Dissipation of k (kg m^{-1} s^{-3})
Y_ω	Dissipation of ω (kg m^{-3} s^{-2})

Abbreviation

BOG	Boiling-Off Gas
CFD	Computational Fluid Dynamics
CCS	Cargo Containment System
LNG	Liquefied Natural Gas
RMS	Root Mean Square
SST	Shear Stress Transport
Tcf	Trillion Cubic Feet

Subscript

m	Mixture
d	Droplet
evap	Evaporated
s	Solid
sec	Secondary barrier layer
pri	Primary barrier layer
use	Utilization
v or vap	Vapour

Greek symbols

α	Volume fractions of phase
γ	The relaxation time factor(s^{-1})
ε	Accumulated root-mean-square
η	The utilization coefficient
η_{use}	Cooling energy utilization ratio
η_{evap}	LNG droplet evaporated ratio
λ	Fluid thermal conductivity (W m^{-1} K^{-1}
μ	Viscosity of the fluid (Pa s)
Γ_k	Effective diffusivity of k (Pa s)
Γ_ω	Effective diffusivity of ω (Pa s)
ρ	Density (kg m^{-3})
$\vec{g}$	The gravitational acceleration (m s^{-2})

1. INTRODUCTION

The intense push to pursue cleaner energy resources during the last decade for the purpose of environmental protection has resulted in the consumption of natural gas worldwide is projected to increase from 120 trillion cubic feet (Tcf) in 2012 to 203 Tcf in 2040 (EIA, 2016). The amount of the LNG transported by ship carriers has grown seven times faster than the amount of LNG transported by pipeline, and it is predicted that by 2035 its proportion will reach approximately 50% (BP 2017), compared to 32% today. There are 452 LNG carriers being operated around the world, and 112 LNG carriers have been ordered to be built. The expansion of LNG carriers is expected to continue in the future due to the sharp increase in the demand for LNG transportation (Raju et al, 2016; Ekanem Attah and Bucknall, 2015).

When using carriers to transport LNG, safety issues must be considered (Lee et al, 2011; Harris, 1993; Horvat, 2018; Fulford and Slatter, 1988). The aim of the cooling down operation is to cool down the tanks in accordance with specifications. This operation is carried out immediately after the completion of the gassing-up in which the inert gas is purged with BOG to prevent the high freezing material from blocking the valves and equipment (WMT Limited 2009; Jia et al 2013; CHINA CLASSIFICATION SOCIETY 2014). Rapid cooling could significantly weaken the strength of the construction (Zhu et al 2018b; Zhu et al, 2018a), which might leads to a critical condition of the cargo containment system (CCS) (Luo, 2011).

To ensure safe operations, it is necessary to understand the heat transfer mechanisms of the cooling down process (Castillo and Dorao 2013; Wang et al 2018; Qu et al, 2018; Yan et al, 2016; Krikkis, 2018). No experimental test data or comprehensive theoretical analysis regarding this topic has been reported due to the extremely high cost and the complicated process. Therefore, numerical simulations were chosen as the basic tools to investigate the flow and heat transfer in the tanks (Peng et al, 2019; Saleem et al, 2018a; Saleem et al, 2018b). The scientific literature on numerical simulations for LNG tanks cover different methods, including the lumped parameter method (LPM) (Luo, 2011; Cui, 2001; Li, 1996) and computational fluid dynamics (CFD) simulations (Wang et al, 2010; Lu et al, 2016a; Zhang and Wu 2014; Lee et al, 2015; Lu, 2012). Cui (2001) and Li (1996) developed a cooling down prediction technology for Moss spherical tanks (Niu, 2017) (which are the product by Moss, Norway) based on the LPM. This method assumed that the temperatures of the fluid inside the cargo tanks and that of the tank wall were uniforms with zero thermal gradient. The equation of the thermal equilibrium was based on the principle of energy conservation between the vapour inside the tank and the barriers of the tank, and the equation was solved through iteration. This method fundamentally ignored the temperature variations inside the cargo tanks and the CCS.

The primary advantage of the LPM is time-saving. However, its prediction tends to have a greater derivation from the measured values because of its oversimplified assumptions. Lu (2012) conducted an unsteady 3D numerical simulation of the cooling down process of membrane cargo tanks by using the versatile CFD software ANSYS-FLUENT. The temperature field, velocity field, coolant particle streamline and vapour volume fraction contour of the fluid inside the cargo tank were systematically investigated. However, the heat transfer between the liquid in the cargo tank and the walls of the tank has not yet been considered and the latent heat caused by the phase transition has been ignored.

The Lee model (Lee, 1980) has been widely utilized to model the phase transition (from liquid to vapour) model to date, and it has been applied in the CFD simulations (Lu et al, 2016a; Zhang and Wu, 2014; Liu et al, 2014). However, the derivation of the results varied widely from the measured data because of the improper equation used to calculate the state of the gas. Moreover, only the thermal conductivity process of insulation materials was presented in their studies, and the risks of the vapour pressure, temperature histories, and optimization temperature were not considered.

Two major issues have been widely ignored in the existing models and the approaches to predict the thermodynamics associated with the cooling down operation. The first issue is the suitable gas law, which could accurately predict the pressure risk inside the tank. The second issue involves operation economics. The negative gauge pressure due to the violent evaporation of the LNG droplets should be accurately predicted because it could result in the inward collapsing of the invar membranes since the barriers are located on the outside of the tank without any support from the inside of the invar membranes. The pressure oscillation inside the tank during the rapid cooling down process could destroy the vapour header, the LNG header, and the tank. The conservation of time and the resources by the cooling down operation leads to the improvement of the economics (Wilson, 1974). This also justifies the necessity of developing a reliable and efficient numerical approach to predict the thermodynamics associated with the cooling down operation (Al-Sharafi et al, 2017), contributing to the decision-making process for an optimized cooling down plan.

In this paper, a CFD model to simulate the flow and heat transfer of the cooling down process is presented. The incompressible ideal gas law is applied to compute the density and pressure accurately. The temperature, density, and pressure of the vapour and the temperature histories of the insulation layers are then analysed. The inwards collapsing risk of the invar membranes due to the negative gauge pressure is identified, and proposals are presented. The heat transfer characteristics of the primary and secondary barriers are also discussed, and based on the discussion, and the proposal of suggested option is introduced.

2. MODEL AND VERIFICATION

2.1 PHYSICAL MODEL

An LNG carrier tank of 14,000m^3 capacity is shown schematically in Figure 1. The X-Y plane is the horizontal plane, with the X-axis oriented along the length of the tank. The cross section is an octagon in the Y-Z plane. The characteristic dimensions are also shown in this figure. The tank is supported by the LNG CCS. Generally, an LNG CCS consists of a thin, flexible membrane called the primary membrane, which is in contact with the cargo, a layer of plywood boxes filled with Perlite called the primary insulation, a second flexible membrane similar to the first one called the secondary membrane, and a second layer of boxes also filled with Perlite in contact with the inner hull called the secondary insulation (WMT Limited, 2009; Lu et al, 2016b). In these layers, the primary and secondary insulation layers act as barriers, and they are mainly insulation layers.

The two invar membrane layers are the leakage prevention layers whose thermal expansion coefficients is very small, its thermal expansion coefficients are about one-tenth of the thermal expansion coefficients 304 type's stainless steel. The thicknesses of the primary and secondary barriers are 230mm and 300mm, respectively. The coolant LNG droplets are sprayed from the liquid header which is defined as the velocity inlet in the model. The vapour header, which is defined as the pressure outlet, is located in the middle of the liquid header. The liquid header and vapour header are located in the middle of the roof of the tank.

It was feasible to construct a simplified computational domain to reduce the computational *run-time* by taking advantage of the following facts that: (i) The thicknesses of the tank primary barrier invar membranes are very small (0.7 mm) and their thermal conductivity is very large. Thus, the invar membranes are ignored in the heat-transfer model. (ii) The physical properties of the materials of the insulation layers and those of the carrier's inner-hull are steady. (iii) The vapour density is in accordance with the incompressible ideal gas law, the vapour density difference is 170% when the temperature reduces from 300 K to 110 K, whereas the vapour density difference is only 1.8% when the pressure changes from 7000 Pa to 9000 Pa. therefore the effect of pressure change on the vapour density can be ignored. (iv) The temperature of the outside of the inner-hull is assumed to be constant at 300 K. (v) Only half of the cargo is modeled because of the symmetry of the physical and geometrical characteristics.

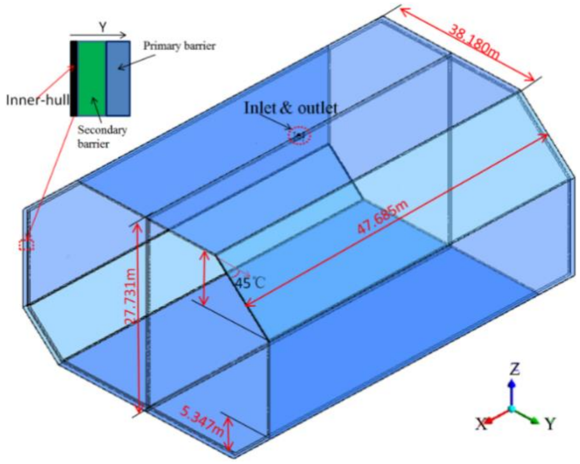

Figure 1: Physical model of the liquid cargo tank

The material properties of the model and the LNG flow rate at different cooling times are shown in Table 1 (Choi et al, 2012) and Table 2 (WMT Limited, 2009), respectively.

2.2 MATHEMATICAL MODEL

The mixture model is chosen because it is a perfect substitute for the full Eulerian multiphase model when there is a wide distribution of the particulate phase. In this process, there are two phases: the vapour occupies most volume of the tank, it is set as the primary phase, and the liquid droplets are set as the secondary phase. The vapour and droplet phases are subscripted as v and d, respectively. The mixture phase, subscripted as m, is the combination of the vapour and droplet phases.

The multi-phase mixture model solves the continuity, momentum, and energy equations for the mixture and the volume fraction equations for the secondary phase/phases (Patankar, 1980; Veersteg and Malalasekera, 1995). The governing equations include (1) the mass conservation of the mixture:

$$\frac{\partial \rho_m}{\partial t} + \nabla \cdot \left(\rho_m \vec{v}_m \right) = 0 \tag{1}$$

Table 1. The material properties of fluids and solids

	Material	Density (kg/m^3)	Specific heat $(J/(kg \cdot k))$	Viscosity $(kg/m \cdot s)$	Thermal conductivity $(w/(m \cdot k))$	Latent heat (kJ/kg)
Fluid	LNG	---	3408	0.1176	0.186	511.15
	Vapour	variable	2222	1.087×10^{-5}	variable	---
Barriers	Expanded Perlite	50	487	---	variable	---
Inner-hull	Steel	8130	480	---	13.8	---

Where ρ_m is the density of the mixture in kg/m^3, t is the time in s, $\vec{v}_{\mathrm{m}}$ is the mixture's mass-averaged velocity in m/s.

The volume fraction equations for the primary and secondary phases are described as follows:

$$\begin{cases} \dfrac{\partial\left(a_{\mathrm{d}}\rho_{\mathrm{d}}\right)}{\partial t}+\nabla\cdot\left(a_{\mathrm{d}}\rho_{\mathrm{d}}\vec{v}_{\mathrm{m}}\right)=-\nabla\cdot\left(a_{\mathrm{d}}\rho_{\mathrm{d}}\vec{v}_{\mathrm{dr,d}}\right)+\left(\dot{m}_{\mathrm{vd}}-\dot{m}_{\mathrm{dv}}\right) \\ a_{\mathrm{v}}=1-a_{\mathrm{d}} \end{cases} \tag{2}$$

Where ρ_d is the density of the droplet in kg/m^3, α_d and α_v are the Volume fractions of phase droplet and vapour respectively, $\vec{v}_{\mathrm{dr,d}}$ is the drift velocity of phase droplet in m/s, $\dot{m}_{\mathrm{vd}}$ and $\dot{m}_{\mathrm{dv}}$ are Synchronized phase transitions from vapour to droplet and droplet to vapour respectively in kg/s.

The momentum and energy equations of the mixture phase are then solved:

$$\begin{aligned} &\frac{\partial\left(\rho_{\mathrm{m}}\vec{v}_{\mathrm{m}}\right)}{\partial t}+\nabla\cdot\left(\rho_{\mathrm{m}}\vec{v}_{\mathrm{m}}\vec{v}_{\mathrm{m}}\right)= \\ &-\nabla p+\nabla\cdot\left(\mu\nabla\vec{v}_{\mathrm{m}}+\nabla\vec{v}_{\mathrm{m}}{}^{T}\right)+\rho_{\mathrm{m}}\vec{g}+\vec{F} \end{aligned} \tag{3}$$

and

$$\begin{aligned} &\frac{\partial\left(\rho_{\mathrm{m}}E_{\mathrm{m}}\right)}{\partial t}+\nabla\cdot\left(\vec{v}_{m}\left(\rho_{\mathrm{m}}E_{m}+p\right)\right)= \\ &\nabla\cdot\left(k_{\mathrm{eff}}\nabla T\right)+S_{T} \end{aligned} \tag{4}$$

Where p is the static pressure in *Pa*, $\vec{g}$ is the gravitational acceleration in m/s^2, $\vec{F}$ is the external body forces in *N*, E_m is the volume average energy of mixture in *J/m*^{3}, k_{eff} is the effective heat transfer coefficient in *W/(m*^{2}*·K)*, S_T is the heat source due to the phase change in *W*.

The shear-stress transport (SST) $\kappa-\varpi$ model (Menter, 1994) was developed to effectively blend the robust and accurate formulation of the $\kappa-\varpi$ model in the near-wall region with the free stream independence of the $\kappa-\varepsilon$ model in the far field region. This is more accurate and reliable for this simulation.

$$\frac{\partial(\rho k)}{\partial t}+\frac{\partial\left(\rho k u_{\mathrm{j}}\right)}{\partial x_{\mathrm{j}}}=\frac{\partial}{\partial x_{\mathrm{j}}}\left[\Gamma_{\mathrm{k}}\frac{\partial k}{\partial x_{\mathrm{j}}}\right]+G_{\mathrm{k}}-Y_{\mathrm{k}} \tag{5}$$

$$\frac{\partial(\rho\varpi)}{\partial t}+\frac{\partial\left(\rho\varpi u_{\mathrm{j}}\right)}{\partial x_{\mathrm{j}}}=\frac{\partial}{\partial x_{\mathrm{j}}}\left[\Gamma_{\omega}\frac{\partial\varpi}{\partial x_{\mathrm{j}}}\right]+G_{\omega}-Y_{\omega} \tag{6}$$

Where k and ω are the turbulence kinetic energy in m^2/s^2 and the specific dissipation rate in 1/s respectively, Γ_k and Γ_ω are the effective diffusivity of k and the effective diffusivity of ω in *Pa.s* respectively, G_k and G_ω are the generation of k in kg/(m·s^3) and the generation of ω in kg/(m^3·s^2) respectively, Y_k and Y_ω are the dissipation of k in kg/(m·s^3) and the dissipation of ω in kg/(m^3·s^2) respectively.

A mass transfer model describing the process of evaporation and condensation that was introduced by Lee (Lee, 1980) has been proven to be robust. In this model, the mass transfer between phases was dependent on the saturation temperature, T_{sat}. The directions and magnitudes of the mass transfer rates are described as follows: evaporation occurs when $T > T_{sat}$. The mass of the liquid phase in the control volume decreases, but the mass of the vapour phase increases correspondingly, which means the mass is transferred from the liquid to the vapour. The synchronized phase transitions from vapour to droplet and from droplet to vapour are shown below.

$$\begin{cases} \dot{m}_{\mathrm{dv}}=\gamma\alpha_{\mathrm{d}}\rho_{\mathrm{d}}\dfrac{T-T_{\mathrm{sat}}}{T_{\mathrm{sat}}},T>T_{\mathrm{sat}} \\ \dot{m}_{\mathrm{vd}}=0,T>T_{\mathrm{sat}} \end{cases} \tag{7}$$

Where γ is the relaxation time factor in 1/s, T and T_{sat} are the temperature and the saturation temperature in *K* respectively.

Similarly, condensation occurs when $T < T_{sat}$. The mass of the liquid phase in the control volume increases, but the mass of the vapour phase decreases correspondingly, which means the mass is transferred from the vapour to the liquid. The magnitude of the mass transfer is

$$\begin{cases} \dot{m}_{\mathrm{vd}}=\gamma\alpha_{\mathrm{v}}\rho_{\mathrm{v}}\dfrac{T_{\mathrm{sat}}-T}{T_{\mathrm{sat}}},T<T_{\mathrm{sat}} \\ \dot{m}_{\mathrm{dv}}=0,T<T_{\mathrm{sat}} \end{cases} \tag{8}$$

Where ρ_v is the density of the vapour in kg/m^3.

The coefficient γ needs to be fine-tuned and can be interpreted as the relaxation time factor that controls the strength of the phase transition. The value of γ varies for different situations. An excessively large value of γ can cause a number of convergence problems, while an overly values can result in a significant deviation between the interfacial temperature and the saturation temperature. The value of γ was specified as 0.1 s^{-1} when the process of LNG evaporation (T_{sat}= 110 K) was simulated by Lu (2016b). In this simulation, γ=0.1 s^{-1} will also be used.

As long as the mass source term is obtained, the energy source term can be obtained by taking the latent heat during the phase change into account. The latent heat at a given temperature of the liquid due to the phase transition in this model is constant. The energy source term due to the phase transition denoted as S_{T}, is calculated as follows:

$$S_{\mathrm{T}}=h_{\mathrm{d}}\left(\dot{m}_{\mathrm{dv}}-\dot{m}_{\mathrm{vd}}\right) \tag{9}$$

Where h_d is the latent heat of phase transformation in *J/kg*.

For the cooling down process, the vapour density is affected more by the temperature change rather than by the pressure change. Therefore, the incompressible ideal gas law was applied to compute the density. In this form, the vapour density only depends on the operating pressure instead of on the local gauge pressure.

$$\rho_v = \frac{P_{op}}{RT / M_W} \tag{10}$$

Where P_{op} is the operation pressure that was set as 8000 Pa (WMT Limited, 2009), R is the universal gas constant that is 8.31 J/(mol·k), and M_w is the CH_4 in kg/mol.

In the inner hull, for the primary barrier and the secondary barrier, only the energy conversion equations were solved, which have the following forms:

$$\frac{\partial(\rho_s h)}{\partial t} = \nabla(k_s \nabla T) \tag{11}$$

and

$$h_s = \int_{T_{ref}}^{T} C_p dT \tag{12}$$

Where ρ_s is the density of material of hull, primary barrier and the secondary barrier in kg/m^3, k_s is conductivity of solid material in *W/(m·K)*, h_s is the sensible enthalpy of solid material in *J/kg*, C_p is the specific heat of solid material in *J/(kg·K)*.

2.3 SIMULATION CONDITION AND MESH

The spraying nozzle boundaries were set to be velocity inlets passing through the LNG with variable volumes, which are shown in Table 2, and the coolant temperature was 110 K. The outlet was set to be a wall because the safety valve could not be opened when the gauge pressure was lower than 25000 Pa (WMT Limited, 2009). The interfaces between the fluid and the primary barrier, the primary barrier, and the secondary barrier, and the secondary barrier and the hull were set to the coupled interface boundary conditions, which allowed for heat flux through the interfaces. An atmosphere temperature of 300 K was given to the outside of the hull wall boundary.

At the initial period, the tank was filled with 300 K boiling off gas (BOG) whose pressure is 8000 Pa in the fluid zone (WMT Limited, 2009), and the temperature of all barriers and the hull was 300 K. The non-uniform unstructured tetrahedron mesh was created by GAMBIT software and then converted to a polyhedron mesh by Fluent, the images of mesh are shown in Figure 2. The total number of mesh cells was approximately 2×10^5, and an initial grid sensitivity study demonstrated that the grid enables accurate prediction of the flow and heat transfer parameters.

Table 2. The LNG flow rates at different cooling times

Cooling down time (h)	LNG flow rate (m^3/h)
0≤t<2	50
2≤t<12	70

2.4 TIME-STEP SIZE AND GRID SENSITIVITY

In addition to the base grid described in the previous section, two more grids were generated with a $\sqrt{2}$ refinement ratio. One of them was a coarser grid with 140,000 cells, and the other was a finer grid with 280,000 cells. The base time step was set as 18s. For the assessment of the time-step size dependence, two more time-step sizes were tested, a larger one, 20s, and a smaller one, 16s. Table 3 shows the results of the dependence tests. The results are represented by the accumulated root-mean-square (RMS) (Lee et al, 2011) values of the temperature differences of the primary and secondary barriers over the entire computation time.

$$\varepsilon = \frac{1}{N}\sum_{n=1}^{N}\sqrt{\left(\frac{T_1-T_2}{T_2}\right)^2} \tag{13}$$

Where ε is accumulated root-mean-square, N and n are the count of temperature, T_1 and T_2 are correlation data of temperature and baseline data of temperature in K respectively.

Note that the accumulation was done by adding in a discrete sense, i.e., every 5 min. From Table 3 it can be clearly seen that the differences were quite small, and the solutions were independent of the grids and time-step sizes in the tested range.

Table 3. Time-step size and grid dependence test

	Primary barrier	Secondary barrier
ϵ_{grid}(Coarse − Medium)	2.10×10^{-2}	3.88×10^{-3}
ϵ_{grid}(Medium − Fine)	8.87×10^{-3}	2.67×10^{-3}
$\epsilon_{time\ step\ size}$(Large − Medium)	1.61×10^{-3}	2.69×10^{-4}
$\epsilon_{time\ step\ size}$(Medium − Small)	8.27×10^{-4}	1.45×10^{-4}

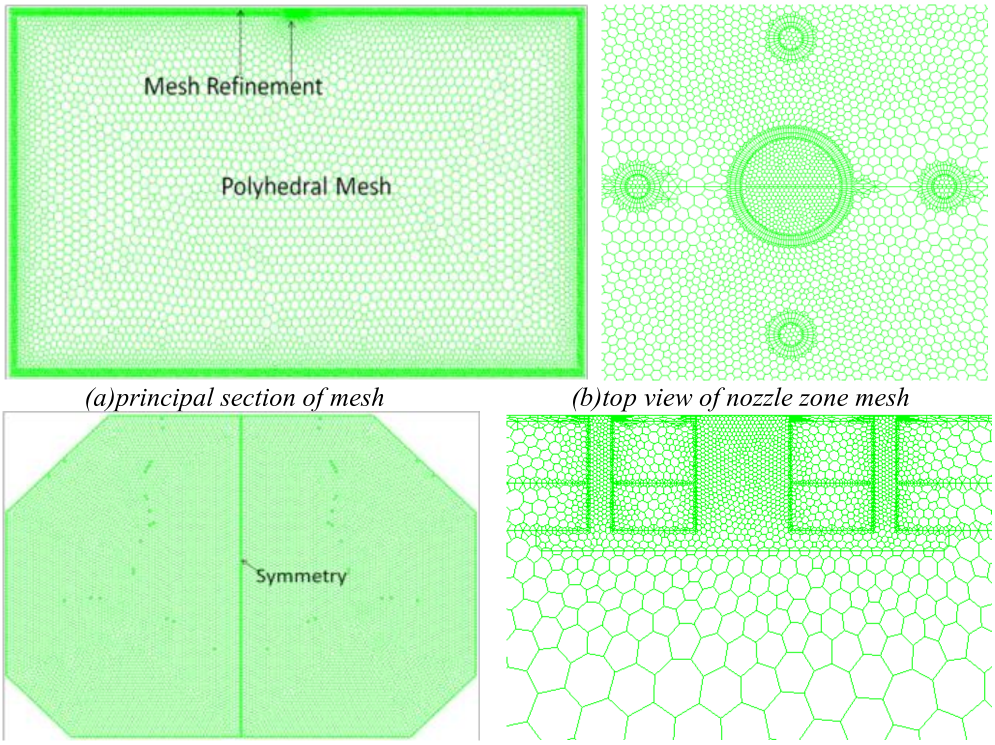

Figure 2: Mesh generation for the computational domain

2.5 EXPERIMENTAL VALIDATION

A cooling down test of a prototype LNG carrier cooling down test (WMT Limited, 2009), carried out by WMT was simulated using the proposed model, and the simulation results were compared with the test data. The simulation results were compared with the test data of the prototype LNG carrier for validation, and the comparison of the time histories of the mean temperatures of the primary barrier is shown in Figure 3. It can be observed that the CFD model slightly underestimated the temperature initially and then overestimated it. However, the gradually reducing trend was clear.

Considering the complexity of the numerical modeling, reasonable simplification and difficulty in the measurement, it was agreed that the results were acceptable. Although there were some discrepancies between the CFD predictions and the experimental measurements, the CFD model showed an acceptable performance. The time-varying temperature was successfully predicted. This indicates that the proposed numerical methods can be used to simulate the LNG carrier.

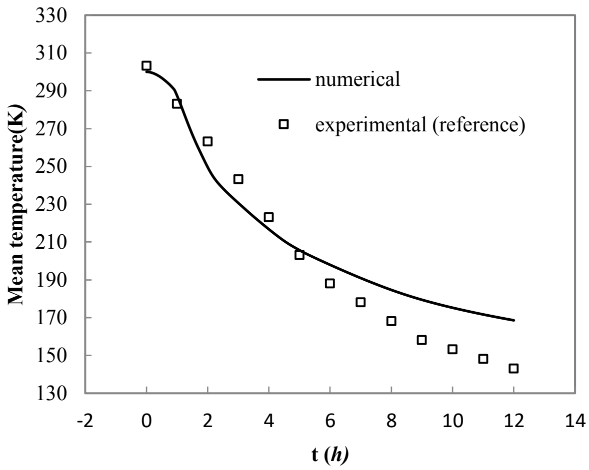

Figure 3: The comparison of the mean time-varying temperature of the primary barrier

To better understand the heat transfer mechanism during the cooling down process, the cooling energy utilization ratio (η_{use}) and the LNG droplet evaporated ratio (η_{evap}) were studied:

$$\eta_{\text{use}} = Q_2 / Q_1 = (Q_1 - Q_3) / Q_1 \tag{14}$$

$$\eta_{\text{evap}} = m_2 / m_1 \tag{15}$$

Where η_{use} is the cooling energy utilization ratio, η_{evap} is the LNG droplet evaporated ratio, Q_1 is the heat transfer rate that input to from the current layer in *W*, Q_2 is the heat transfer rate that output from the current layer in *W*, Q_3 is the residual heat of the current layer in *W*, m_1 is the injected

3. RESULTS AND DISCUSSION

In this section, the temperature, density, and pressure characteristics of the vapour inside the tank are analysed based on the model, and the temperature histories of the different barriers, as well as the heat transfer characteristics between layers, are shown and discussed. The mean velocity, temperature, density, pressure of vapour is calculated based on the volume-weighted average of the variable on a 3D location.

LNG masses for each hour in kg, m_2 is the evaporated LNG masses for each hour in kg.

The heat transfer coefficient K (Miana et al, 2016) and the Nusselt number Nu are defined by the following expressions.

$$K = Q / \left(A \cdot \Delta T \right) \tag{16}$$

and

$$Nu = \frac{K.L}{\lambda} \tag{17}$$

Where K is the heat transfer coefficient in $W/(m^2 \cdot K)$, Q is the net heat transfer rate between two contiguous layers in W, A is the heat exchange area in m^2, ΔT is the difference of the average temperature for the adjacent layers in K, Nu is the Nusselt number, L is the hydraulic diameter in m, λ is the fluid thermal conductivity in $W/(m \cdot K)$.

As LNG droplets were sprayed into the tank, the LNG droplets flash evaporated due to the violent heat transfer from the hot vapour. The vapour was cooled down by the LNG droplets, and then the barriers were cooled down synchronously by the cold vapour.

3.1 VAPOUR COOLING ANALYSIS

The vapour changes which include the density, the temperature, and the pressure were analysed and discussed. The time-varying mean temperature and the density, as well as pressure histories of the vapour, are shown in Figure 4. The temperature of the primary barrier and the temperature differences of the primary barrier and the vapour are also included in Figure 4 for comparison. The temperature, density and velocity distributions comparison at a different time in middle sections of the tank are shown in Figure 5, Figure 6 and Figure 8 respectively. The heat transfer rate, the evaporated and cooling utilization ratios, the Nusselt number, and the velocity histories of the vapour are shown in Figure 7.

It was found that there were two significantly different periods for the temperature and density histories of the vapour in Figure 4(a). Specifically, the temperature of the vapour underwent an initial sharp drop and the density of the vapour increased linearly during the first period ($t < 2.3$h). Due to the almost constant heat sink, which is caused by the constant LNG spray amount during this period, the slopes of the temperature vs. time curve stayed at about -91.60K/h. And the slopes of the vapour density vs. time curve keeps at 0.55kg/m^3.h because of the almost constant temperature decrease slope. The vapour average temperature dropped from 300 K to 215.22 K at 0.5h and 116.80 K at 2h (Figure 5) during this period, and the vapour density increased from 0.70kg/m^3 to 0.98kg/m^3 at 0.5h and 1.80kg/m^3 at 2h (Figure 6). The huge temperature *differences* between vapour and LNG droplets (110K) leads to a strong heat transfer rate, which tends to result in flash evaporation of LNG with the same spray amount cryogenic coolant droplets injection. Consequently, the vapour temperature of the vapour dropped at a constant slope, and the vapour density increased at a constant slope. In the second period ($t > 2.3$h), the vapour temperature and density are no longer changing.

The gauge pressure history of the vapour inside the tank is shown in Figure 4(b). It was found that the mean gauge pressure declined sharply to -120 Pa from 0 Pa at the initial period. Then the relative pressure increased linearly and reached 0 Pa at the 1.64th hour. At the end of the cooling down process, the relative pressure reached 527.85 Pa. The relative pressure increased with a constant slope due to the almost constant LNG volume of LNG injection. The final absolute pressure (8527.85 Pa) of the vapour doesn't exceed the outlet (safety valve) opening limit (25000 Pa) during the whole cooling down process, so the boundary condition setting of the outlet in this mode is acceptable.

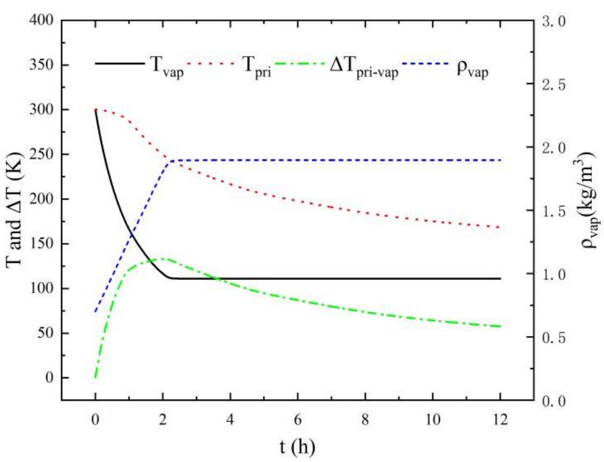

(a) The histories of temperature, temperature differences, and density

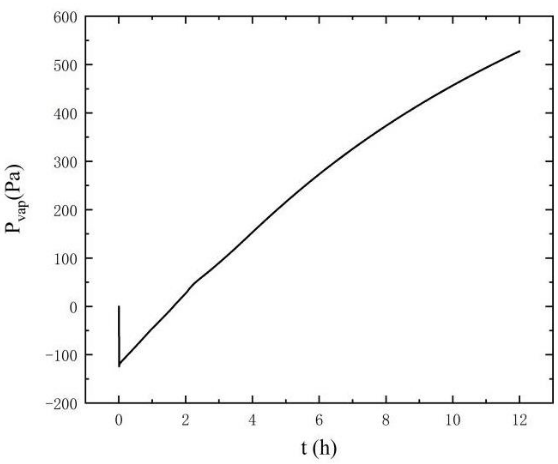

(b) Mean pressure histories

Figure 4: The mean temperature, density and pressure histories of the vapour

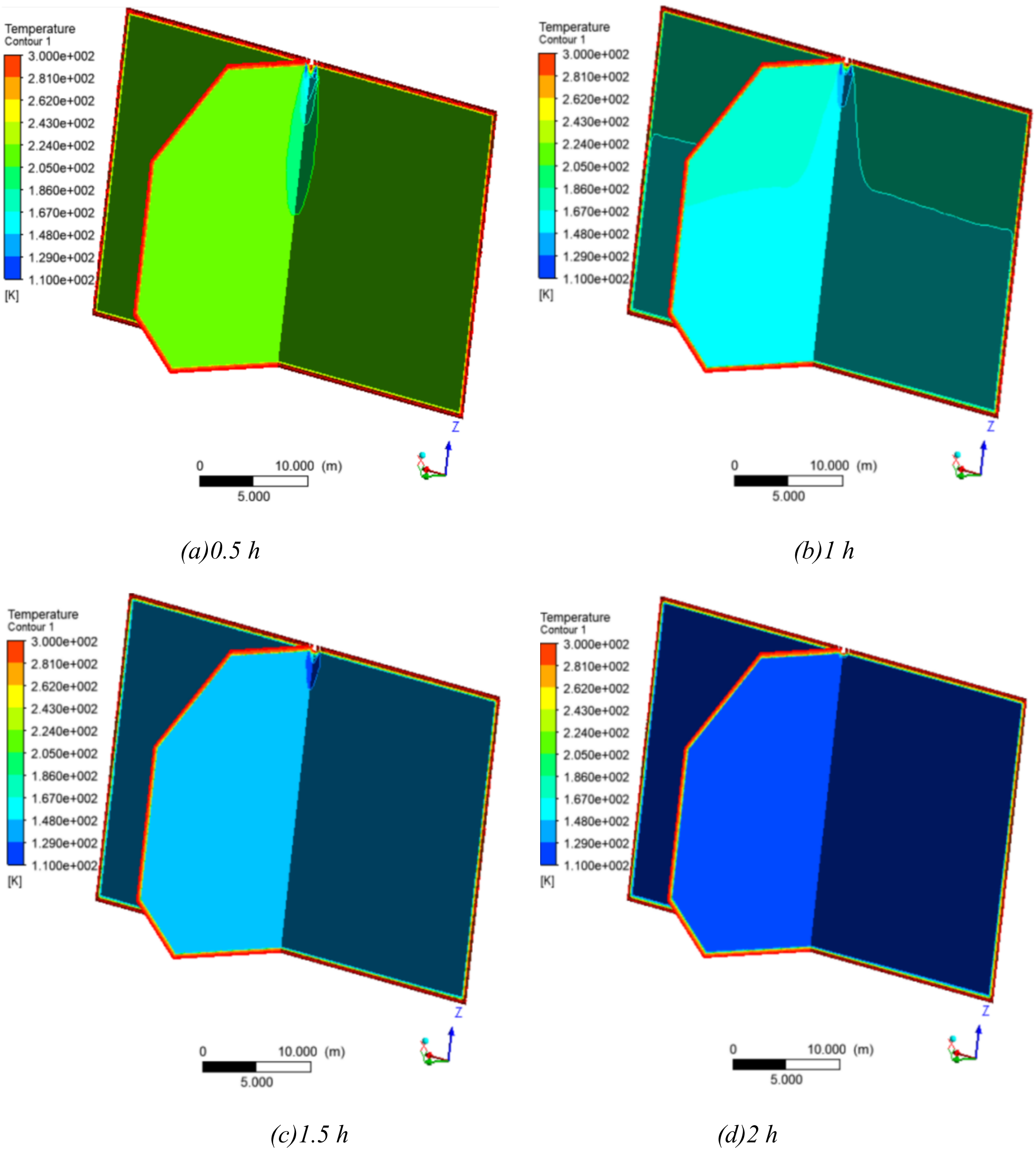

Figure 5: The temperature distribution comparison in middle sections of the tank

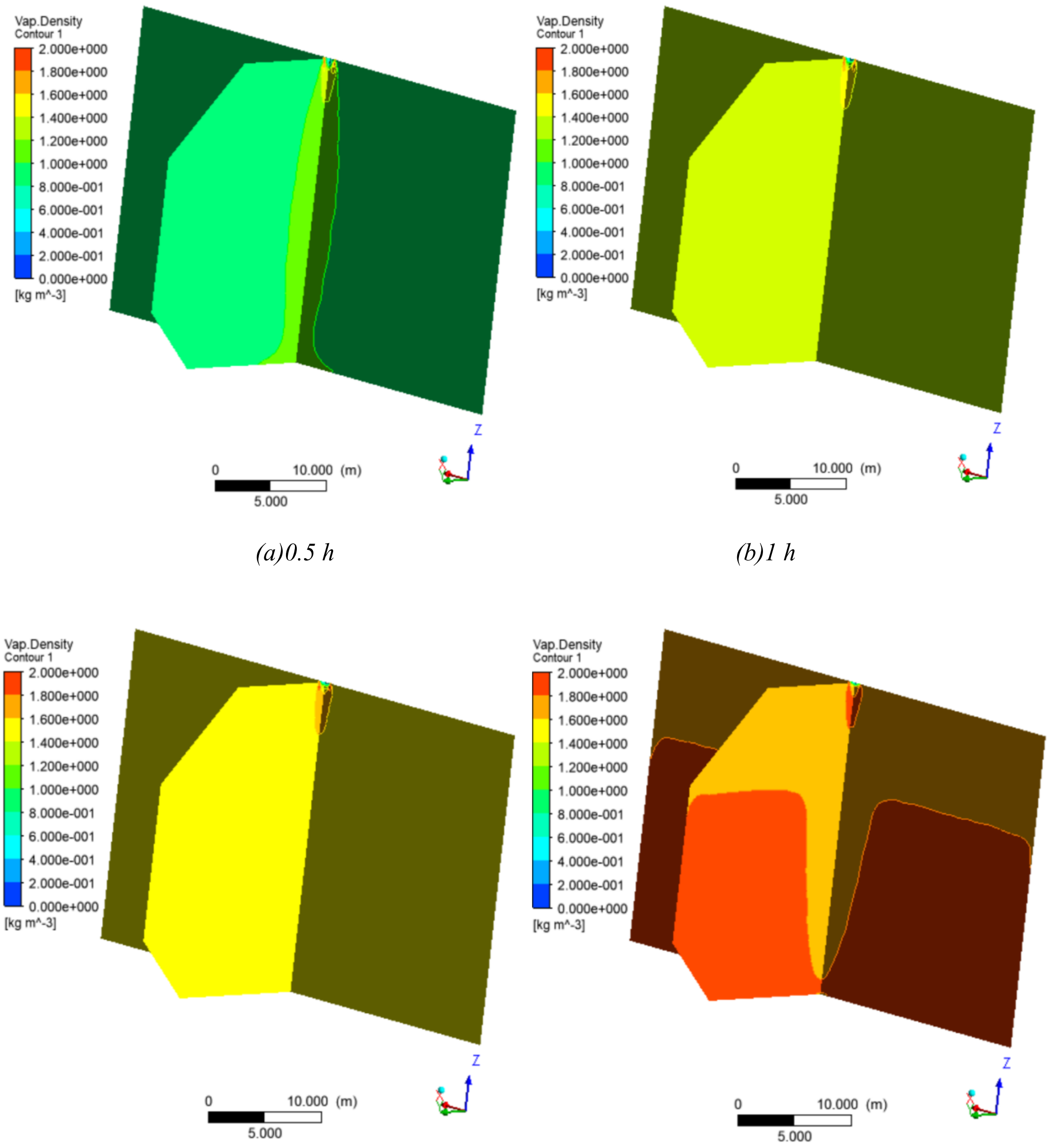

(a)0.5 h *(b)1 h*

(c)1.5 h *(d)2 h*

Figure 6: The vapour density distribution comparison in middle sections of the tank

The LNG droplet evaporation ratios experienced three distinct stages, as shown in Figure 7 - namely the fast cooling stage, the transition cooling stage, and the stable cooling stage. The fast cooling stage (first stage) lasted about 1.5 hours. In this stage, the injected LNG droplets fully evaporated (Figure 7(a)) because the vapour temperature was sufficiently high. Meanwhile, the vapour velocity caused by LNG evaporation and heat transfer between vapour and the primary barrier is relatively intense (Figure 8(a)), hence the vapour velocity is rapidly increased to a high level and the Nu number have the similar trend as the vapour velocity (Figure 7(b)). After 1h, the temperature difference between the LNG droplets and the vapour reduces to 45.5 k. Although the LNG droplets still could be fully evaporated, the evaporation and heat transfer caused vapour velocity and the Nu number are reduced (Figure 7(b)). In the fast cooling stage, the heat transfer rate between the vapour and the primary barrier increases rapidly and then keeps at 1.80×10^5 W for about half an hour.

From expression (16) and (17),

$$Nu = Q\frac{L}{(A \cdot \Delta T)\lambda} \tag{18}$$

Where L is the characteristic length which is a constant, λ almost keep constant, A is the characteristic area size which is a constant and ΔT is the temperature different which can be found from Figure 4.(a). So Nu number behaves similarly to the rate of heat transfer Q, which is increase when the velocity increases. In the period, the Nu number of the heat transfer between vapour and primary barrier have the similar trend as the heat transfer rate, due to the rapidly increasing of the velocity.

From 1.5 h to 2.5 h, the injected LNG droplets evaporation ratio sharply decreases from 100% to 30% (Figure 7(a)). The vapour average velocity and the Nu number are fallen to the lowest values (Figure 7(b)) due to the lowest temperature different of vapour and LNG droplets, which causes the heat transfer rate between the vapour and primary barrier sharply decrease by 53% to 8.51×10^4 W (Figure 7(a)). This stage is defined as the transition cooling stage because the cooling capacity has degenerated.

The third stage is the stable cooling stage, which continues from the 2.5th hour to the end. Before this stage, the vapour was cooled to near the saturation temperature (Figure 4(a)), hence the LNG droplets' evaporated ratio slowly declined to 10%. The vapour velocity and the Nu number stay very small (Figure 7(a)) because of the low LNG droplets' evaporated ratio, which causes the lower heat transfer rate between the vapour and LNG droplets.

There are two heat sources for LNG droplets evaporation. One part comes from the vapour itself and another is from the primary barrier which is transferred by vapour. The ratio of heat come from vapour itself in the total heat is marked as cooling energy utilization ratio of the vapour, and the cooling energy utilization of the vapour itself is shown in Figure 7(a) which is as high as 96.63%. The majorities (96.63%) of the heat come from the vapour itself, and only a very small part of the heat comes from the barrier.

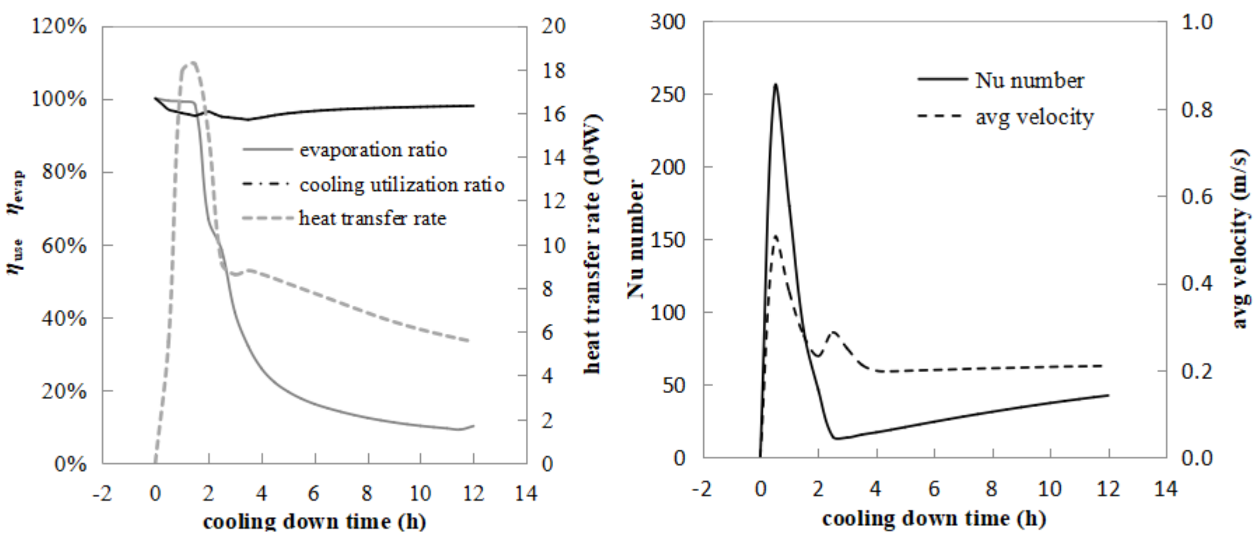

(a) The evaporated, cooling utilization ratios and heat transfer rate between the barrier and the vapour

(b) The Nu number and the volume average velocity

Figure 7: The evaporated and cooling utilization ratios, the Nu number and the velocity histories of the vapour

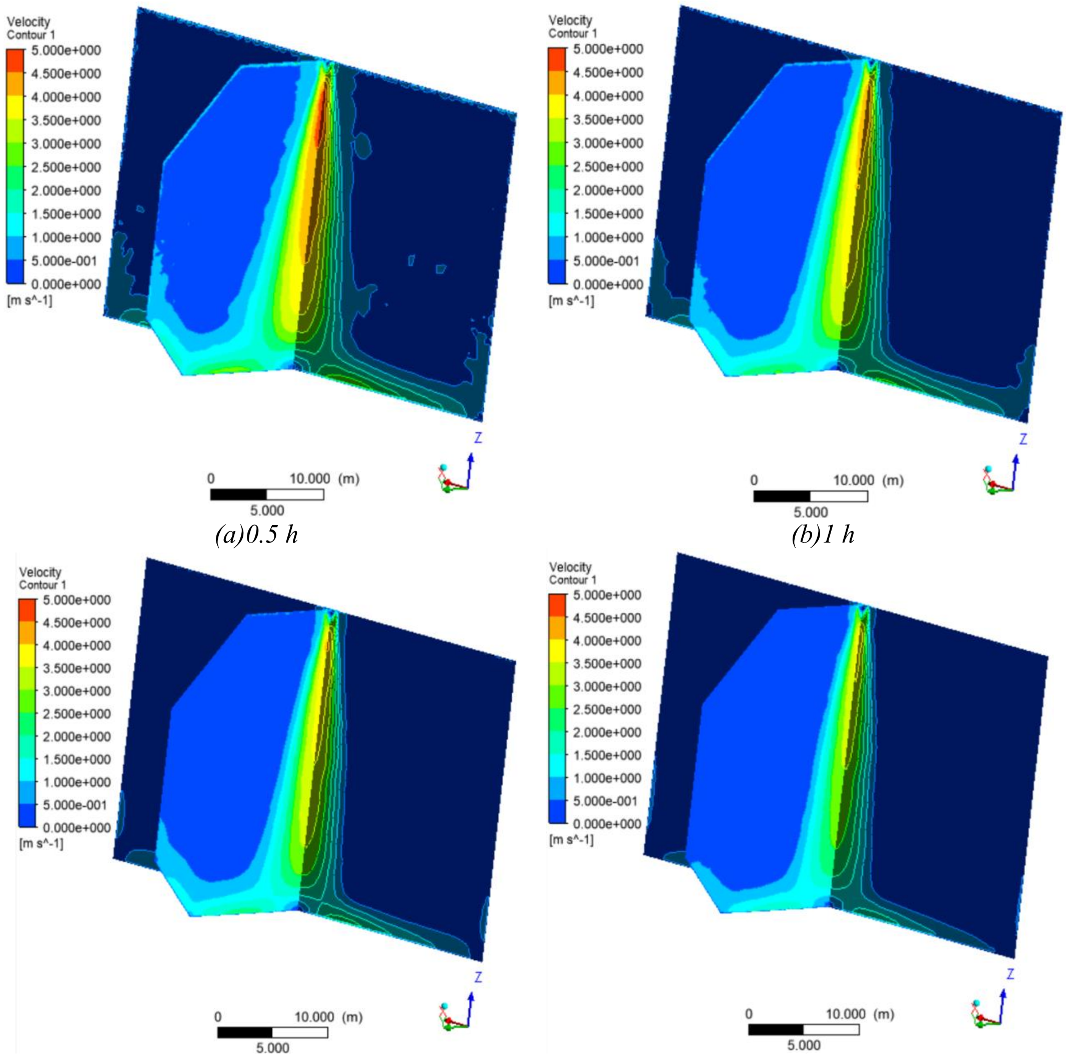

(a)0.5 h *(b)1 h*

(c)1.5 h *(d)2 h*

Figure 8: The mixture velocity distribution comparison in middle sections of the tank

3.2 PRIMARY BARRIER COOLING CHARACTERISTIC ANALYSIS

The LNG droplets are the final thermal sink of the heat from the barriers and vapour. The heat of the primary barrier is controlled by the convective heat transfer from the vapour inside the tank and the heat conduction from the secondary barrier.

The time-varying temperature and the temperature profiles at a different time of the different layers are shown in Figure 9. The heat transfer rate and the heat transfer coefficients of the different interfaces are shown in Figure 10 and the cooling energy utilization coefficient is shown in Figure 11. The heat transfer of the primary barrier has different characteristics in different periods. It can be found in these Figures that:

(1) The temperature of the primary barrier drops with the vapour temperature.

(2) There are three significantly different stages of the heat transfer rate between the primary barrier and the vapour inside the tank, which are the fast heat transfer period, the transition period, and the stable heat transfer period.

The fast heat transfer stage starts from the beginning and continues for 1.5h. The heat transfer rate and heat transfer coefficients (Figure 10) of vapour and primary barrier are intensely higher than those of the primary and secondary barriers during this period. The volume average velocity and the Nu number are sharply increased to their maximum values (Figure 7), therefore, convection heat transfer dominates the heat transfer at this stage. Convective heat transfer often referred to simply as convection, is the transfer of heat from one place to another by the movement of fluids, which is more efficient than heat conductivity. Therefore, the convective heat transfer mechanism is a reasonable explanation for this intensely higher heat transfer rate.

From 1.5h to the 3.0h, the heat transfer rate from the primary barrier to vapour inside the tank decreases by 50%, from 1.82×10^5 W to 8.62×10^4 W, which is defined as the transitory stage. In this stage, the Nu is gradually decreased, leading to a reduction of convective heat transfer. Simultaneously, conductive heat transfer becomes increasingly dominant.

Generally, the convective and conductive heat transfer mechanisms have a comparable important position in this stage.

After 3h, the heat transfer rate from the primary barrier to the vapour decreases to the same level as the heat transfer rate from the secondary barrier to the primary barrier. The overall heat transfer coefficient (Miana et al, 2016) of the two sides of the primary barrier is at the same level, and the heat transfer is controlled by conductive accordingly.

(3) Consequently, there are three different stages of the temperature changes in the primary barrier, which are the rapid cooling stage, the stable cooling stage, and the slow cooling stage.

In the rapid cooling stage, the heat transfer rate is intensely higher than that of the primary and secondary barriers, from the beginning to 3.25h. Accordingly, the temperature of the primary barrier drops rapidly. This temperature drop is mainly controlled by the temperature of the vapour. The cooling energy utilization coefficient is higher, and the cooling energy utilization coefficient has the lowest value during this period, 74.3%.

In the stable cooling stage, the temperature difference between the primary barrier and the vapour becomes lower with the heat transfer mechanism transition; the heat transfer rate sharply declines and the temperature gradient of primary barrier consequently decreases. The cooling energy utilization coefficient drops to 24.7% during this period, which is a decrease of 50%.

The third stage is the slow cooling stage. In this stage, the heat transfer efficiency of the two sides of the primary barrier is at the same level, and the temperature gradient is extremely small. The cooling energy utilization coefficient drops to 13.0%. The primary barrier becomes extremely hard to cool.

The heat transfer rate between the primary barrier and the vapour drops rapidly from 1.6×10^5 W to 8×10^4 W after 7.25 h. Accordingly, the injection coolant can be reduced by 50% to economize. The comparison of the LNG flow rate between baseline and suggested option is shown in Table 3. In the suggestion option, 210 m^3 of the coolant can be saved and the economical ratio is 26.3%.

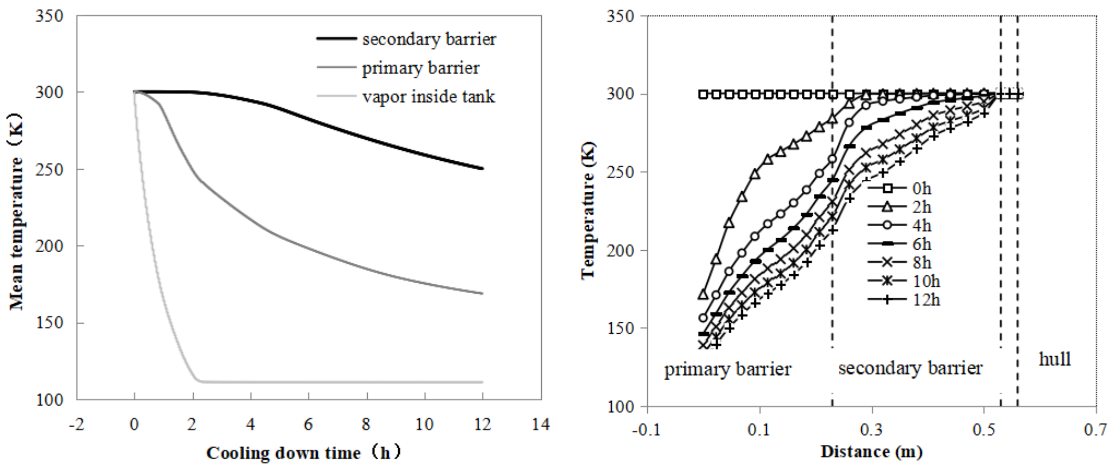

(a) Temperature histories *(b) Temperature profiles*

Figure 9: The temperature histories and temperature profiles of different layers

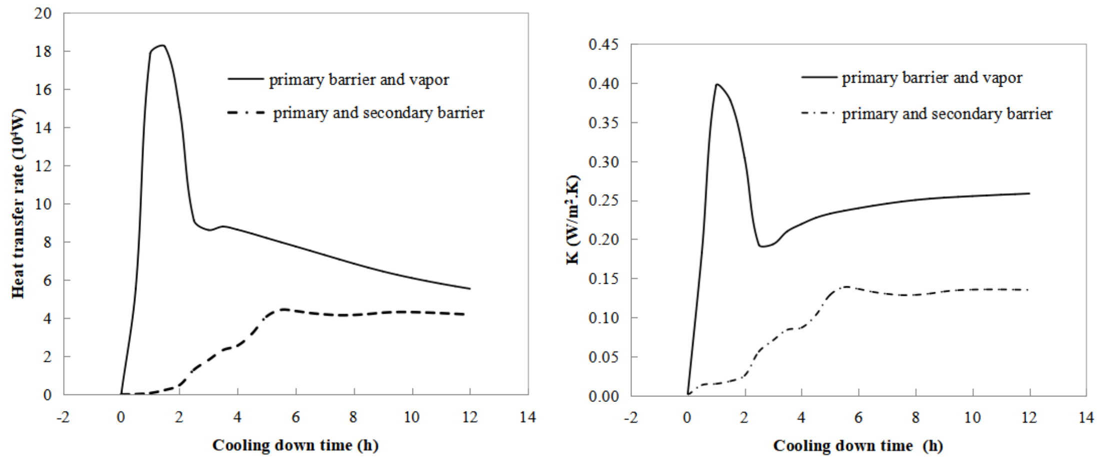

(a) Heat transfer rate *(b) Heat transfer coefficients*

Figure 10: The heat transfer rate and coefficients of different layers of primary barrier cooling

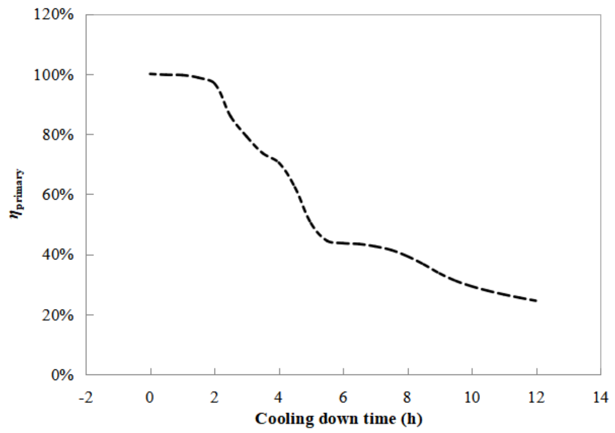

Figure 11: The cooling energy utilization coefficient of the primary barrier

3.3 SECONDARY BARRIER COOLING CHARACTERISTICS ANALYSIS

Conductive dominate the heat transfer in the secondary barrier, and it includes the conductive heat from the primary barrier and the inner hull. The cooling characteristics are different from the primary barrier because of the different heat transfer mechanism. The temperature and temperature difference histories of the different layers associated with the cooling of the secondary barrier are shown in Figure 12. The heat transfer rate through the different layers and the cooling energy utilization coefficient associated with the cooling of the secondary barrier are shown in Figure 13.

From Figure 12 and 13, the cooling characteristics of the secondary barrier are shown as follows.

1) The temperature of the secondary barrier drops due to the drop in the temperature of the primary barrier.
2) The heat transfer mechanisms of the secondary barrier from the two side layers are conductive, and consequently, the heat transfer rate (Figure 12(a)) is mainly controlled by the temperature difference (Figure 12(b)). The curves of the temperature difference and the heat transfer rate have the same tendency.
3) The temperature difference between the secondary barrier and inner hull becomes higher, and accordingly, the heat transfer rate from the inner hull to the secondary barrier becomes higher. The cooling energy utilization coefficient drops to 61.2% during the cooling process.

3.4 TOTAL COOLING ENERGY UTILIZATION COEFFICIENT

The total cooling energy utilization coefficients of the combination of the primary and secondary barriers are shown in Figure 14. It can be seen there are two different stages of the total cooling energy utilization coefficient during the cooling process.

1) In the high-efficiency cooling stage, from the beginning to the 4th h, the cooling energy utilization coefficient is very high and the lowest cooling energy utilization coefficient is 94.8%. Up to 94.8% of the cooling energy is used to cool the barriers.
2) In the utilization rate of the decline stage, from 4th h to the end, the cooling energy utilization coefficient declines The lowest cooling energy utilization coefficient is 70.7%, and the mean cooling energy utilization coefficient is 88.7%. During this stage, 88.7% of the cooling energy which transfers from vapour is used to cool the barriers.

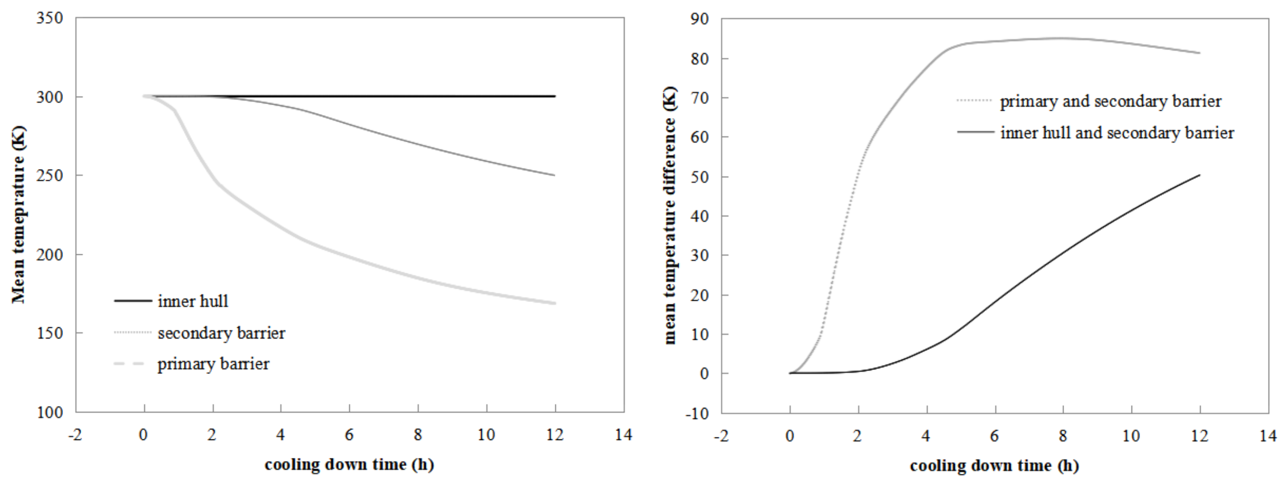

(a) Mean temperature *(b) Mean temperature difference*

Figure 12: The temperature and temperature difference histories of the different layers of cooling for the secondary barrier

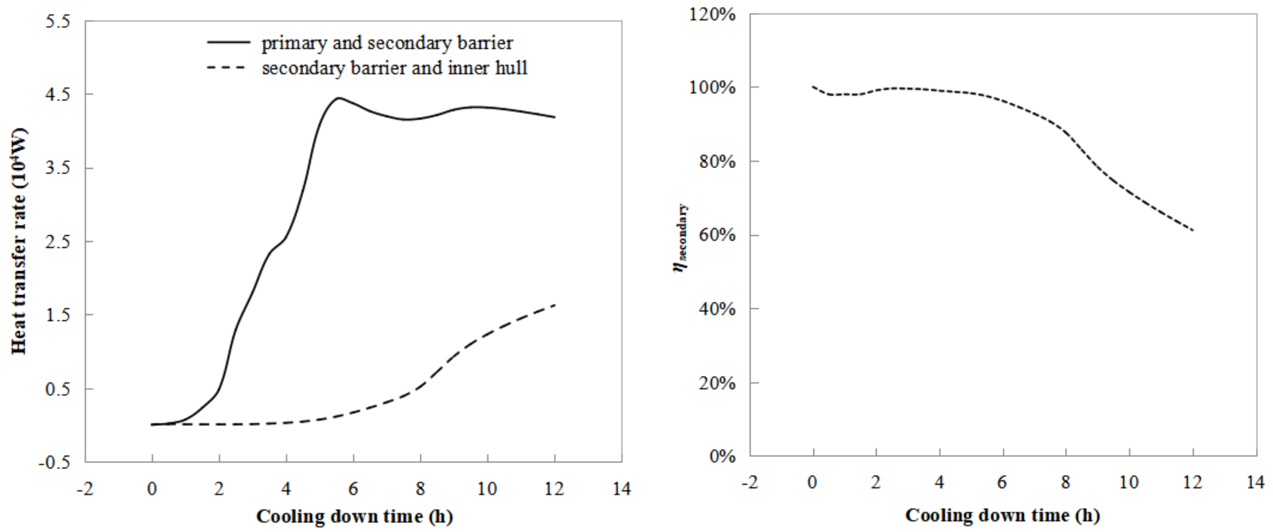

(a) Heat transfer rate *(b) Cooling energy utilization coefficient*

Figure 13: The heat transfer rate of the different layers and cooling energy utilization coefficients of the secondary barrier

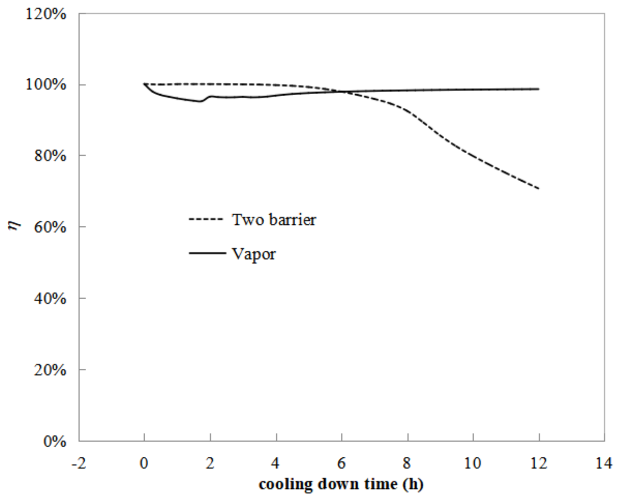

Figure 14: Cooling energy utilization coefficient of the two barriers and the vapour

4. OPERATION PROPOSALS

The LNG evaporation ratio sharply declined when the vapour temperature dropped to near 110K after 2 hours, thus a reduced injected LNG amount was available to save the LNG. A simulation of the suggested option was conducted, in which the sprayed LNG was reduced by 50% from the 3rd hour to the end. The comparisons of the LNG flow rate between baseline and suggested option are shown in Table 4.

The vapour pressure and temperature comparisons between baseline and suggested option are shown in Figure 15 and 16, and the RMS is shown in Table 5. The vapour pressure decreased from the 3rd hour due to the reduction of the LNG flow rate, but the temperature differences between the baseline and suggested option and the RMS values were very small. The suggested option has almost the same cooling down performance as the baseline, so it is acceptable and feasible. It saved 315m^3 of the LNG in suggested option and the saving ratio was 39.38%.

Table 4. The LNG flow rate comparison between the baseline and the suggested option

Cooling down time (h)	LNG flow rate (m^3/h)	
	baseline	suggested option
$0 \leq t < 2$	50	50
$2 \leq t < 3$	70	70
$3 \leq t < 12$	70	35
Total	800	485

Table 5. The RMS of the baseline and suggested option data

	RMS
T_{Vapour}	7.81×10^{-4}
ρ_{Vapour}	7.86×10^{-4}
P_{Vapour}	2.95×10^{-1}
$T_{\text{Primary barrier}}$	1.02×10^{-2}
$T_{\text{Secondary barrier}}$	1.40×10^{-3}
$T_{\text{Inner hull}}$	1.12×10^{-7}

The negative relative pressure could result in an inwards collapsing risk for the invar membranes because the barriers are located at the outside of the tank but without any support inside the tank. The pressure oscillation risk, caused by negative relative pressure overlying due to multi tanks cooling down at the same time, could destroy the vapour header, the LNG header, and the tank. For safe operation and risk avoided several proposals are shown as follows:

1) It is essential to monitor the gauge pressure inside the tanks carefully, and the emergency response measures

should be predefined and prepared. Cryogenic BOG is a possible alternative coolant for the initial period; another possible alternative involves tuning the injection LNG droplets amounts to avoid negative relative pressure. Another choice would be to inject BOG from the vapour header during the initial period, which is able to keep the relative pressure positive.

2) Avoid launching the cooling down process for multi tanks at the same time. The middle tank is recommended for the first launch, while the other tanks work as buffer tanks via the vapour valves that are kept always opened and connected to the vapour headers. It is suggested that these tanks be launched one by one. The next tank should be launched one hour after the last cooling tank relative pressure reaches 0 Pa. This launching rhythm will help to avoid the pressure oscillation risk.

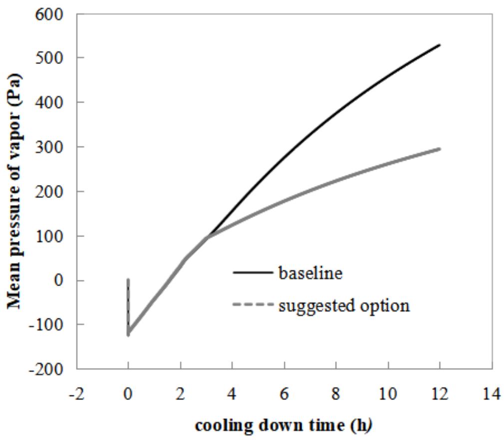

Figure 15: Comparison of the baseline and optimized mean pressures of the vapour

5. CONCLUSION

A multiphase CFD model was presented to simulate the phase change and heat transfer of the cooling down process of a single cargo tank. The temperature, density, and pressure of the vapour inside the tank and the heat transfer characteristics of the primary and secondary barriers have been comprehensively analysed, and the proposals have been presented.

1) The predicted results show good agreement with the measured data, with a maximum bias of 12.8%.
2) The temperature of the vapour drops from 300K to 110K and the density of the vapour increases from 0.70 kg/m^3 to 1.89 kg/m^3 in 2.3 h. The slopes of the time-varying temperature and density curves change with constant slopes during this period; the slopes are -48.7 K/h and 0.31 kg/m$^3\cdot$h for the temperature and the density, respectively.
3) The relative pressure declines sharply to -120 Pa at the initial period, then the relative pressure increases with a constant slope and reaches 0 Pa at 2.9 h, and at the end of the cooling down process, the relative pressure reaches 527.85 Pa. The maximum absolute pressure (8527.85 Pa) of the vapour doesn't exceed the outlet (safety valve) opening limit (25000 Pa), so the wall boundary condition setting of the outlet is acceptable.
4) The cooling process of the primary barrier has three different periods, which are the rapid cooling period, stable cooling period, and the slow cooling period, because of the three significantly different heat transfer mechanisms.

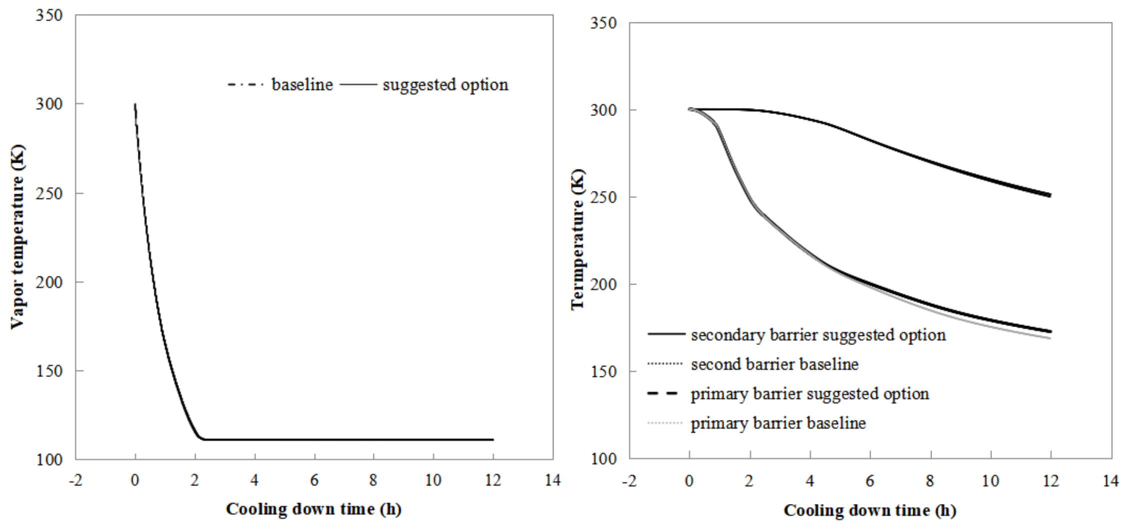

(a) Vapour temperature *(b) The temperature of the barriers*

Figure 16: Comparison of the baseline and suggested option barrier temperatures

5) The heat transfer mechanism of the secondary barrier from the two side layers is conductive. Consequently, the heat transfer rate is mainly controlled by the temperature difference. The cooling energy utilization coefficient drops to 61.2% during the cooling process.
6) Up to 94.8% of the cooling energy was used for cooling the barriers from 0 to 4h, the cooling energy utilization coefficient dropped to 70.7%, and the mean value was 88.7% from 4h to the ending.

Based on the calculation results analysis, the proposals for the safety operations and saving costs are shown as follows.

1) Carefully monitor the gauge pressure and the emergency response should be predefined. The cryogenic BOG is an alternative coolant for the initial stage, or for tuning the injection LNG amounts.
2) Avoid launching the cooling down process for multi tanks at the same time. The middle tank is recommended for the first launch. The tanks launch one by one, this launching rhythm will help to avoid the pressure oscillation risk.
3) The injection coolant can be reduced by 50% after 3 hours because of the sharp decrease of the heat transfer rate from the primary barrier to the vapour inside the tank. The coolant mounts can be saved by 315 m^3, and the economical ratio is 39.38%.

6. ACKNOWLEDGMENTS

This work was supported by a Project supported by the National Science Foundation for Young Scholars of China (Grant No.11602222), the Zhejiang basic public welfare research project (Grant No.LY18E090009), Zhoushan City Technology Bureau Project Funding (Grant No.2016C41021).

7. REFERENCES

1. AL-SHARAFI, A., YILBAS, B. & ALI, H. 2017. *Heat Transfer and Fluid Flow Characteristics in a Sessile Droplet on Oil-Impregnated Surface Under Thermal Disturbance*. Journal of Heat Transfer, 139(9), 1-49.
2. BP. 2017. *BP Energy Outlook 2017 edition* [Online]. Available: http://www.bp.com/content/dam/bp/pdf/energy-economics/energy-outlook-2017/bp-energy-outlook-2017.pdf [Accessed 2017].
3. CASTILLO, L. & DORAO, C. A. 2013. *On the conceptual design of pre-cooling stage of LNG plants using propane or an ethane/propane mixture*. Energy Conversion and Management, 65, 140-146.
4. CHOI, S. W., ROH, J. U., KIM, M. S. & LEE, W. I. 2012. *Analysis of two main LNG CCS (cargo containment system) insulation boxes for leakage safety using experimentally defined thermal properties*. Applied Ocean Research, 37, 72-89.
5. CUI, Y. 2001. *The liquid cargo technology of LNG carrier and the thermodynamic study of the pre-cooling process.* Master, Shanghai Maritime University.
6. EIA, U. S. 2016. International Energy Outlook 2016. Washington, DC: U.S. EIA.
7. EKANEM ATTAH, E. & BUCKNALL, R. 2015. *An analysis of the energy efficiency of LNG ships powering options using the EEDI*. Ocean Engineering, 110, 62-74.
8. FULFORD, N. J. & SLATTER, M. D. 1988. *Developments in the safe design of LNG tanks*. Cryogenics, 28, 810-817.
9. HARRIS, F. S. 1993. *Safety features on LNG ships*. Cryogenics, 33, 772-777.
10. HORVAT, A. 2018. *CFD methodology for simulation of LNG spills and rapid phase transition (RPT).* Process Safety and Environmental Protection, 120, 358-369.
11. JIA, S., LV, J. & DENG, Q. 2013. *A simulation study of boil-off gas (BOG) pre-cooling process in unloading pipelines in an LNG terminal in Zhejiang*. Natural Gas Industry, 33, 84-88.
12. KRIKKIS, R. N. 2018. *A thermodynamic and heat transfer model for LNG ageing during ship transportation. Towards an efficient boil-off gas management.* Cryogenics, 92, 76-83.
13. LEE, H. B., PARK, B. J., RHEE, S. H., BAE, J. H., LEE, K. W. & JEONG, W. J. 2011. *Liquefied natural gas flow in the insulation wall of a cargo containment system and its evapouration*. Applied thermal engineering, 31, 2605-2615.
14. LEE, J. H., KIM, Y. J. & HWANG, S. 2015. *Computational study of LNG evapouration and heat diffusion through a LNG cargo tank membrane*. Ocean Engineering, 106, 77-86.
15. LEE, W. H. 1980. *A Pressure Iteration Scheme for two-phase flow modeling,* Washington D C, Hemisphere Publishing.
16. LI, P. 1996. *On the pre-cooling temperature of spherical cargo tank for MOSS type LNG Carrier*. Journal of Shanghai Maritime University, 17, 73-78.
17. LU, J., XU, S., DENG, J., WU, W., WU, H. & YANG, Z. 2016a. *Numerical prediction of temperature field for cargo containment system (CCS) of LNG carriers during pre-cooling operations*. Journal of Natural Gas Science and Engineering, 29, 382-391.
18. LU, J. S., XU, S., DENG, J. J., WU, W. F., WU, H. X. & YANG, Z. B. 2016b. *Numerical prediction of temperature field for cargo containment system (CCS) of LNG carriers during pre-cooling operations*. Journal of Natural Gas Science and Engineering, 29, 382-391.

19. LU, W. 2012. *Study on the pre-cooling process of membrane liquid cargo tank of LNG Carriers.* Master, Dalian Maritime University.
20. LUO, T. 2011. *Study on unsteady heat transfer of pre-cooling process of Large-Scale LNG Storage Tank.* Master, Lanzhou University of Technology.
21. MENTER, F. 1994. *Two-Equation Eddy-Viscosity Transport Turbulence Model for Engineering Applications*. AIAA Journal, 32.
22. MIANA, M., LEGORBURO, R., DíEZ, D. & HWANG, Y. H. 2016. *Calculation of Boil-Off Rate of Liquefied Natural Gas in Mark III tanks of ship carriers by numerical analysis*. Applied Thermal Engineering, 93, 279-296.
23. PATANKAR, S. V. 1980. *Numerical heat transfer and fluid flow*, London: Hemisphere Publishing Corporation.
24. PENG, Q., WU, H., WANG, D. W., HE, Y. J. & CHEN, H. 2019. *Numerical simulation of aircraft crash on large-scale LNG storage tank*. Engineering Failure Analysis, 96, 60-79.
25. QU, Y., NOBA, I., XU, X., PRIVAT, R. & JAUBERT, J.-N. 2018. *A thermal and thermodynamic code for the computation of Boil-Off Gas–Industrial applications of LNG carrier*. Cryogenics, 99, 105-113.
26. RAJU, T. B., SENGAR, V. S., JAYARAJ, R. & KULSHRESTHA, N. 2016. *Study of Volatility of New Ship Building Prices in LNG Shipping*. International Journal of e-Navigation and Maritime Economy, 5, 61-73.
27. SALEEM, A., FAROOQ, S., KARIMI, I. A. & BANERJEE, R. 2018a. *CFD simulation of a full scale LNG storage tank*. San Diego, the United States, 1-5 July 2018. Amsterdam: Elsevier.
28. SALEEM, A., FAROOQ, S., KARIMI, I. A. & BANERJEE, R. 2018b. *A CFD simulation study of boiling mechanism and BOG generation in a full-scale LNG storage tank*. Computers & Chemical Engineering, 115, 112-120.
29. CHINA CLASSIFICATION SOCIETY. 2014. 《 RULES FOR CONSTRUCTION AND EQUIPMENT OF SHIPS CARRYING LIQUEFIED GASES IN BULK 》. Beijing: CHINA CLASSIFICATION SOCIETY.
30. VEERSTEG, H. K. & MALALASEKERA, W. 1995. *An Introduction to Computational Fluid Dynamics: The Finite Volume Method*. Pearson Schweiz Ag, 20, 400.
31. WANG, J., LI, Y., WANG, L., ZHU, K., XIE, F. & LI, C. 2018. *Transient modeling of cryogenic two-phase flow boiling during chill-down process*. Applied Thermal Engineering, 143, 461-471.
32. WANG, Z., LI, P. & JIN, G. 2010. *CFD simulation for coolant of LNG carrier in pre-cooling process.* Journal of Shanghai Maritime University, 31, 49-53.
33. WILSON, J. J. 1974. *An introduction to the marine transportation of bulk LNG and the design of LNG carriers.* Cryogenics, 14, 115-120.
34. WMT LIMITED, U. 2009. *Dapeng Moon Cargo Operating Manual*. Hong Kong.
35. YAN, Y., PFOTENHAUER, J. M., MILLER, F., NI, Z. & ZHI, X. 2016. *Numerical study of heat transfer characteristics in BOG heat exchanger*. Cryogenics, 80, Part 1, 97-107.
36. ZHANG, P. & WU, Z. 2014. *Numerical simulation of phase change heat transfer of liquid nitrogen based on Fluent*. Cryo. & Supercond, 42, 26-29.
37. ZHU, K., LI, Y., MA, Y., WANG, L., XIE, F. & WANG, J. 2018a. *Experimental study on cool down characteristics and thermal stress of cryogenic tank during LN2 filling process*. Applied Thermal Engineering, 130, 951-961.
38. ZHU, K., LI, Y. Z., MA, Y., WANG, J. J., WANG, L. & XIE, F. S. 2018b. *Influence of filling methods on the cool down performance and induced thermal stress distribution in cryogenic tank*. Applied Thermal Engineering, 141, 1009-1019.